

## Dispersive coupled-channels optical-model potential with soft-rotator couplings for Cr, Fe, and Ni isotopes

Rui Li,<sup>1</sup> Weili Sun,<sup>2,\*</sup> E. Sh. Soukhovitskiĭ,<sup>3</sup> J. M. Quesada,<sup>4</sup> and R. Capote<sup>5</sup>

<sup>1</sup>Graduate School, China Academy of Engineering Physics, Beijing 100088, China

<sup>2</sup>Institute of Applied Physics and Computational Mathematics, Beijing 100088, China

<sup>3</sup>Joint Institute for Energy and Nuclear Research, Minsk-Sosny 220109, Belarus

<sup>4</sup>Departamento de Física Atómica, Molecular y Nuclear, Universidad de Sevilla, Apartado Postal 1065, 41080 Sevilla, Spain

<sup>5</sup>NAPC–Nuclear Data Section, International Atomic Energy Agency, Vienna A-1400, Austria

(Received 20 March 2013; revised manuscript received 16 April 2013; published 17 May 2013)

An approximate Lane-consistent dispersive coupled-channels optical potential is derived that describes nucleon-induced reactions on even iron isotopes. Realistic saturated couplings for <sup>54,56,58</sup>Fe nuclei are built using nuclear wave functions of the soft-rotator model with the Hamiltonian parameters adjusted to reproduce the energy of the low-lying collective levels of these isotopes. *E2*- and *E3*-transition probabilities between low-lying collective levels are well reproduced. The comprehensive experimental database used in the fitting process includes all scattering data for neutron and proton scattering up to 200 MeV on iron nuclei. The derived potential is shown to be applicable to Ni and Cr isotopes, assuming the applicability of the soft-rotator model to these nuclei and to the odd <sup>57</sup>Fe nucleus within the rigid-rotor model. The approximate Lane consistency of the derived potential is validated by describing the quasielastic (*p, n*) scattering with excitation of isobaric analog states. Elastic and inelastic analyzing powers for both neutron- and proton-induced reactions are shown to be in good agreement with experimental data, demonstrating the reliability of the derived dispersive spin-orbit potential.

DOI: [10.1103/PhysRevC.87.054611](https://doi.org/10.1103/PhysRevC.87.054611)

PACS number(s): 24.10.Eq, 24.70.+s, 25.40.Kv, 27.40.+z

### I. INTRODUCTION

Being a major component of steel, iron is the most important structural element in nuclear technology. Chromium (18–20%) and nickel (8–10%) are the other major components of austenitic steels that are widely employed in the nuclear industry. All three materials are therefore important structural materials for nuclear applications. A reduction of the uncertainty of elastic and inelastic scattering data on iron, chromium, and nickel isotopes in the fast neutron region has been requested, therefore motivating additional work on the improvement of phenomenological optical-model potentials for nuclear data modeling and evaluation.

Phenomenological nucleon optical-model potentials (OMPs) that describe successfully the nucleon scattering data have been extensively studied in the past [1]. A widely used one is the global spherical optical potential by Koning and Delaroche [2] for nucleon-induced reactions up to 200 MeV. Recently, more emphasis has been put on the development of the dispersive OMPs proposed and extensively developed by Mahaux and Ngo [3] and Mahaux and Sartor [4,5]. The unified description of the nuclear mean field in the dispersive optical model (DOM) is accomplished by using a dispersion relation, which links the imaginary OMP parts to the corresponding dynamic real parts without requiring additional parameters. Furthermore the dispersive constraint helps to reduce the ambiguities and the number of OMP parameters and also eliminates the need for energy-dependent geometry.

Extensive works on extending the DOM approach into the domain below the Fermi energy by employing additional

experimental data to constrain the potentials have been recently carried out by Morillon and Romain [6], Bespalova and co-workers [7,8], and Dickhoff and co-workers (Ref. [9] and references therein). Progress has been also achieved in the development of the dispersive OMPs for the positive-energy domain that describe nucleon scattering using both spherical [10] and coupled-channels formalism [11–14].

An additional constraint to derived OMP parameters arises from the use of quasielastic (*p, n*) scattering data involving the excitation of isobaric analog states. Such calculations are a good test of the isovector part of the OMP and check for the OMP Lane consistency [15,16]. It has been previously shown by some of the authors [17] that the dispersive coupled-channels optical-model (DCCOM) potential for nucleon-induced reactions on actinides was approximately Lane consistent, but no such a study has been previously undertaken for iron isotopes.

On the other hand, a DCCOM potential for actinides [11,12] used an imaginary spin-orbit potential found by Koning and Delaroche [2], but assumed a dispersive contribution in the real spin-orbit potential that has never been checked by using polarization data (e.g., the analyzing power  $A_y$ ).

Therefore, the aim of the present work is to construct a DCCOM potential for chromium, iron, and nickel isotopes and then perform a joint analysis using almost all types of experimental nucleon-nucleus scattering data, including cross sections, elastic and inelastic angular distributions, quasielastic (*p, n*) data, and analyzing powers. For the latter, a computational method based on the Tamura formalism [18] is given. Such a joint analysis is a good validation for the Lane consistency of the derived DCCOM potential.

This contribution is structured as follows. Section II describes the soft-rotator model analysis. The coupled-channels

\*sun\_weili@iapcm.ac.cn

TABLE I. Assignments of the SRM quantum numbers for the low-lying collective levels of  $^{54,56,58}\text{Fe}$ . Quantum numbers  $n_\gamma$ ,  $n_{\beta_2}$ , and  $n_{\beta_3}$  correspond to the number of  $\gamma$ , quadrupole, and octupole phonons, respectively.  $K$  is the projection of the total angular momentum of the vibrational bandhead (approximate quantum number because strictly speaking  $K$  is not conserved in SRM).

	$^{54}\text{Fe}$	$^{56}\text{Fe}$	$^{58}\text{Fe}$
(i) $K \simeq 0$	$0^+$ (g.s.)	$0^+$ (g.s.)	$0^+$ (g.s.)
$n_\gamma = 0$	$2^+$ (1.408 MeV)	$2^+$ (0.847 MeV)	$2^+$ (0.811 MeV)
$n_{\beta_2} = 0$	$4^+$ (2.538 MeV)	$4^+$ (2.085 MeV)	$4^+$ (2.077 MeV)
$n_{\beta_3} = 0$			
(ii) $K \simeq 2$	$2^+$ (2.959 MeV)	$2^+$ (2.658 MeV)	$2^+$ (1.675 MeV)
$n_\gamma = 0$	$3^+$ (3.345 MeV)	$3^+$ (3.445 MeV)	$3^+$ (2.134 MeV)
$n_{\beta_2} = 0$	$4^+$ (3.835 MeV)		$4^+$ (2.600 MeV)
$n_{\beta_3} = 0$			
(iii) $K \simeq 0$	$0^+$ (2.561 MeV)	$0^+$ (2.942 MeV)	$0^+$ (2.258 MeV)
$n_\gamma = 0$	$2^+$ (3.166 MeV)	$2^+$ (3.748 MeV)	
$n_{\beta_3} = 0$			
$n_{\beta_2} = 1$			
(iv) $K \simeq 0$	$3^-$ (4.782 MeV)	$3^-$ (4.510 MeV)	$3^-$ (3.660 MeV)
$n_\gamma = 0$			
$n_{\beta_2} = 0$			
$n_{\beta_3} = 0$			
(iv) $K \simeq 2$	$3^-$ (6.400 MeV)		
$n_\gamma = 0$			
$n_{\beta_2} = 0$			
$n_{\beta_3} = 0$			

optical-model analysis is presented in Sec. III. Results and discussions are presented in Sec. V. Finally, the summary and conclusions are given.

## II. SOFT-ROTATOR MODEL ANALYSIS

A coupled-channels optical model using matrix elements derived by the soft-rotator model (SRM) [19] is employed to simultaneously describe the low-lying collective level nuclear structure and the nucleon scattering data at positive energies. This approach has been successfully applied to a number of vibrational nuclei, including  $^{58}\text{Ni}$  [19],  $^{56}\text{Fe}$  [20,21], and  $^{52}\text{Cr}$  [22], which are studied in this work.

We first adjusted the SRM Hamiltonian parameters, with the consideration of both quadrupole and octupole dynamic vibrations, to fit the experimentally observed collective levels of  $^{54,56,58}\text{Fe}$  isotopes. The assignments of the SRM quantum numbers for these isotopes using a standard approach [21] are shown in Table I. Such assignments allow us to search for the Hamiltonian parameters; derived parameters for iron isotopes are listed in Table II.

Figure 1 displays a comparison of the calculated and experimental levels of  $^{56}\text{Fe}$  as an example. We show only experimental levels used or predicted by the SRM, while noncollective levels are not shown. One can see that the SRM reproduces well the experimental levels with deviations lower than 10%. The same is true for  $^{54,58}\text{Fe}$  nuclei.

TABLE II. SRM Hamiltonian parameters used to reproduce the experimental level schemes of  $^{54,56,58}\text{Fe}$ .  $\gamma_0$  is the quadrupole nonaxiality parameter;  $\epsilon_0 = \beta_{30}/\beta_{20}$  is the equilibrium octupole deformation. Quantum numbers  $\mu_x$  ( $x = \beta_{20}, \gamma_0, \epsilon$ ) denote the nuclear softness parameter for quadrupole,  $\gamma$ , and octupole phonons, respectively.  $a_{32}$  and  $\eta$  ( $a_{42}, \delta_4$ , and  $\gamma_4$ ) determine the nonaxiality of octupole (hexadecapole) deformations;  $2\delta_n$  is the energy splitting of a doubly degenerated level in octupole vibrations due to the tunneling effect; and the  $\hbar\omega_0$  parameter normalizes the overall scale of the predicted levels.

$^{54}\text{Fe}$			
$\hbar\omega_0 = 1.6630$	$\mu_{\beta_{20}} = 0.9700$	$\mu_{\gamma_0} = 0.7600$	$\gamma_0 = 0.66998$
$a_{32} = 0.004873$	$a_{42} = 0.0053$	$\delta_4 = 0.69718$	$\gamma_4 = 0.093896$
$\mu_\epsilon = 0.65298$	$\eta = 0.0802$	$\delta_n = 7.6615$	$\epsilon_0 = 0.70991$
$^{56}\text{Fe}$			
$\hbar\omega_0 = 2.6016$	$\mu_{\beta_{20}} = 0.48922$	$\mu_{\gamma_0} = 0.1260$	$\gamma_0 = 0.32552$
$a_{32} = 0.004873$	$a_{42} = 0.0$	$\delta_4 = 0.69718$	$\gamma_4 = 0.093896$
$\mu_\epsilon = 0.3500$	$\eta = 0.14557$	$\delta_n = 7.6791$	$\epsilon_0 = 0.85582$
$^{58}\text{Fe}$			
$\hbar\omega_0 = 1.8935$	$\mu_{\beta_{20}} = 0.5439$	$\mu_{\gamma_0} = 0.1260$	$\gamma_0 = 0.42385$
$a_{32} = 0.004873$	$a_{42} = 0.0$	$\delta_4 = 0.69718$	$\gamma_4 = 0.093896$
$\mu_\epsilon = 0.29933$	$\eta = 0.14557$	$\delta_n = 7.3601$	$\epsilon_0 = 0.64596$

Optimal SRM Hamiltonian parameters for Ni isotopes and  $^{52}\text{Cr}$  are listed in Tables III and IV, respectively. A similar level of agreement between SRM calculations and experimental energies is observed for  $^{58,60,62}\text{Ni}$  and  $^{52}\text{Cr}$  nuclei.

Derived deformation parameters  $\beta_{20}$ ,  $\beta_{30}$ , and  $\beta_4$  for even-even Fe isotopes are listed in Table V. Note that only the  $\beta_4$  parameter can be directly related to the similar parameter in the rigid-rotor model.  $\beta_{20}$  and  $\beta_{30}$  cannot be related, because they are the equilibrium quadrupole and octupole deformations (with respect to dynamical soft vibrations), respectively. Therefore, we used two approaches to calculate the effective

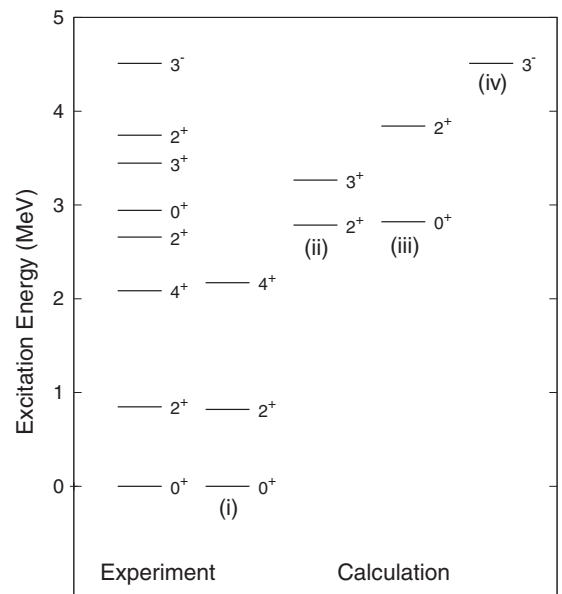


FIG. 1. Comparison of the experimental and predicted level schemes for the  $^{56}\text{Fe}$  nucleus.

TABLE III. SRM Hamiltonian parameters used to reproduce the experimental level schemes of  $^{58,60,62}\text{Ni}$ . Notation is the same as in Table II.

$^{58}\text{Ni}$			
$\hbar\omega_0 = 1.7482$	$\mu_{\beta_{20}} = 1.0239$	$\mu_{\gamma_0} = 0.3900$	$\gamma_0 = 0.6515$
$a_{32} = 0.0001$	$a_{42} = 0.014857$	$\delta_4 = 0.69719$	$\gamma_4 = 0.1141$
$\mu_\epsilon = 0.50193$	$\eta = 0.14194$	$\delta_n = 5.9953$	$\epsilon_0 = 1.0901$
$^{60}\text{Ni}$			
$\hbar\omega_0 = 1.3062$	$\mu_{\beta_{20}} = 1.887$	$\mu_{\gamma_0} = 0.42$	$\gamma_0 = 0.49172$
$a_{32} = 0.0001$	$a_{42} = 0.011933$	$\delta_4 = 0.6974$	$\gamma_4 = 0.11365$
$\mu_\epsilon = 0.43003$	$\eta = 0.10964$	$\delta_n = 6.1169$	$\epsilon_0 = 0.95215$
$^{62}\text{Ni}$			
$\hbar\omega_0 = 1.1794$	$\mu_{\beta_{20}} = 2.7235$	$\mu_{\gamma_0} = 0.63$	$\gamma_0 = 0.29742$
$a_{32} = 0.0001$	$a_{42} = 0.011933$	$\delta_4 = 0.6974$	$\gamma_4 = 0.11365$
$\mu_\epsilon = 0.31179$	$\eta = 0.1044$	$\delta_n = 5.9375$	$\epsilon_0 = 0.69$

deformation parameters, equivalent to those deformation parameters  $\beta_2$  and  $\beta_3$  in the rigid-rotor model. The first approach is to average the equilibrium deformation parameters over the nuclear wave functions of the initial  $|i\rangle$  and final  $|f\rangle$  states, i.e.,  $\beta_2(\beta_3) = \langle i|\beta_{20}(\beta_{30})|f\rangle$ . The wave functions are the eigenfunctions of the SRM Hamiltonian. Such averaging, taking  $\mu_\lambda$  softness to  $\beta_2$  and  $\beta_3$  into account, demonstrates an enhancement of the coupling strength between different channels [19,23]. The second approach is to derive the  $\beta_2$  ( $\beta_3$ ) value from  $B(E2)$  [ $B(E3)$ ] given by the rotational-vibrational model [24,25]. The results are shown in Table VI, together with  $\beta_2$  and  $\beta_3$  determined from experimental  $B(E2)$  and  $B(E3)$ . The effective  $\beta_2$  values calculated by our two approaches is within 5% of those determined from  $B(E2)$  recommended by Raman *et al.* [26]. The effective  $\beta_3$  calculated by  $B(E3)$  is consistent with those recommended by Spear [27], with the largest deviation being lower than 10% for  $^{54,58}\text{Fe}$  nuclei. However, for the case of  $^{56}\text{Fe}$ , the effective  $\beta_3$ , calculated by  $\langle 0_{g.s.}^+|\beta_{30}|3^- \rangle$ , is 0.1537, which is 30% lower than Spear's recommended  $\beta_3 = 0.2145$ . A similar situation has been observed for the  $^{28}\text{Si}$  nucleus in previous work [28], where a possible reason for this discrepancy is discussed.

### III. COUPLED-CHANNELS OPTICAL MODEL ANALYSIS

Coupled-channels calculations were performed with a coupling built on SRM nuclear wave functions with the above SRM Hamiltonian parameters; e.g., eight collective levels were coupled for  $^{56}\text{Fe}$  as shown in Fig. 2. It was verified that the coupling of additional levels changes calculated cross

TABLE IV. SRM Hamiltonian parameters used to reproduce the experimental level scheme of  $^{52}\text{Cr}$ . Notation is the same as in Table II.

$^{52}\text{Cr}$			
$\hbar\omega_0 = 1.4752$	$\mu_{\beta_{20}} = 1.2124$	$\mu_{\gamma_0} = 0.175$	$\gamma_0 = 0.33586$
$a_{32} = 0.0$	$a_{42} = 0.0$	$\delta_4 = 0.69718$	$\gamma_4 = 0.093896$
$\mu_\epsilon = 0.20677$	$\eta = 0.000024$	$\delta_n = 7.3544$	$\epsilon_0 = 0.45$

TABLE V. Static deformation parameters of Fe isotopes.

	$^{54}\text{Fe}$	$^{56}\text{Fe}$	$^{58}\text{Fe}$
$\beta_{20}$	0.131	0.232	0.232
$\beta_{30}$	0.710	0.856	0.646
$\beta_4$	0.109	0.046	0.046

sections within quoted experimental uncertainties. Therefore, we call such a coupling scheme a saturated coupling. Two additional levels were coupled for  $(p, n)$  quasielastic scattering calculations as shown in the top of this figure: The first level is the ground state isobaric analog state (IAS), and the second level is a  $2^+$  excited analog state (EAS).

The energy difference between the ground state of  $^{56}\text{Fe}$  and its corresponding IAS state is just the Coulomb displacement, which can be obtained by the empirical relation [29]  $\Delta_C = 1.444Z/A^{1/3} - 1.13$  MeV, with  $Z$  being the average charge of the target and residual nuclei in the reaction. Note that the energy difference between the analog states in the residual nucleus is kept the same as that between the ground-state rotational band levels in the target nucleus.

The empirical value of  $\Delta_C$  is 8.8719 MeV for  $^{56}\text{Fe}$ . However  $\Delta_C$  can also be given approximately by  $\Delta_C = E_{\text{th}} + E_{\text{ex}}$ , where  $E_{\text{th}}$  is the  $(p, n)$  reaction threshold energy and  $E_{\text{ex}}$  is the measured excited energy of the residual nucleus. For the case of the  $^{56}\text{Fe}(p, n)^{56}\text{Co}$  reaction,  $E_{\text{th}}$  is 5.444 MeV, while the measured  $E_{\text{ex}}$  of  $^{56}\text{Co}$  is 3.5 MeV [30]. Therefore the sum given in such a way is 8.944 MeV, quite close to the empirical one. Similarly, the coupled schemes with the consideration of  $(p, n)$  transitions for  $^{54,58}\text{Fe}$ ,  $^{58,60,62}\text{Ni}$ , and  $^{52}\text{Cr}$  can be built.

A dispersive coupled-channels OMP, taking into account the deformed nuclear shapes, is used in the coupled-channels optical-model calculations. The general formulation with conventional definition of the symbols is given by

$$\begin{aligned}
 V[r, R(\theta', \varphi'), E] &= -[V_{\text{HF}}(E^*)]f_{\text{ws}}[r, R_{\text{HF}}(\theta', \varphi')] \\
 &\quad -[\Delta V_v(E^*) + iW_v(E)]f_{\text{ws}}[r, R_v(\theta', \varphi')] \\
 &\quad -[\Delta V_s(E^*) + iW_s(E)]g_{\text{ws}}[r, R_s(\theta', \varphi')]
 \end{aligned}$$

TABLE VI. The effective deformation parameters  $\beta_2$  and  $\beta_3$  calculated by two approaches as described in the text, together with  $\beta_2$  and  $\beta_3$ , determined from experimental  $B(E2)$  and  $B(E3)$ , respectively.

	$\beta_2$ by $\langle i \beta_{20} f\rangle$	$\beta_2$ by $B(E2)$	$\beta_2$ by $B(E2)$ [26]
$^{54}\text{Fe}$	0.1955	0.1755	0.1958
$^{56}\text{Fe}$	0.2461	0.2645	0.2393
$^{58}\text{Fe}$	0.2543	0.2696	0.2587
	$\beta_3$ by $\langle i \beta_{30} f\rangle$	$\beta_3$ by $B(E3)$	$\beta_3$ by $B(E3)$ [27]
$^{54}\text{Fe}$	0.1193	0.0930	0.1144
$^{56}\text{Fe}$	0.1537	0.1891	0.2145
$^{58}\text{Fe}$	0.1566	0.1807	0.1716

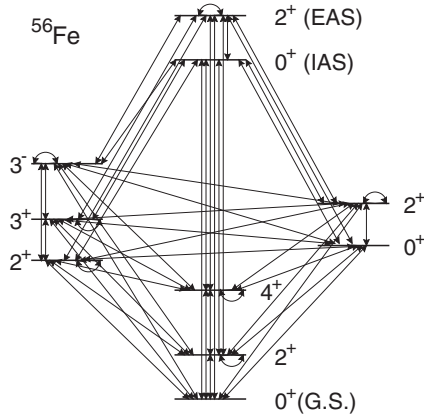


FIG. 2. Coupling scheme used in the coupled-channels calculation for the  $^{56}\text{Fe}$  nucleus.

$$\begin{aligned}
 & + \left( \frac{\hbar}{m\pi c} \right)^2 [V_{\text{so}}(E) + \Delta V_{\text{so}}(E) + iW_{\text{so}}(E)] \\
 & \times \frac{1}{r} \frac{d}{dr} f_{\text{ws}}[r, R_{\text{so}}](\hat{\sigma} \cdot \hat{L}) + V_{\text{Coul}}[r, R_c(\theta', \varphi')], \quad (1)
 \end{aligned}$$

with the geometric form factors given as

$$\begin{aligned}
 f_{\text{ws}}[r, R_i(\theta', \varphi')] &= [1 + \exp[r - R_i(\theta', \varphi')/a_i]^{-1}, \\
 i &= \text{HF}, v \\
 f_{\text{ws}}[r, R_{\text{so}}] &= [1 + \exp[r - R_{\text{so}}/a_{\text{so}}]^{-1}, \\
 g_{\text{ws}} &= -4a_s \frac{d}{dr} f[r, R_s(\theta', \varphi')], \quad (2)
 \end{aligned}$$

where the “effective” nucleon energy  $E^* = E_n$  for neutrons and  $E^* = E_p - E_{\text{Coul}}$  for protons, which accounts for the Coulomb shift due to the repulsion by the target nucleus. The effective energy  $E^*$  for protons is discussed in more detail later. The expressions of the Hartree-Fock (HF) potential,  $V_{\text{HF}}(E)$ , the imaginary and corresponding dispersive potentials  $W_i(E)$  and  $\Delta V_i(E)$ , ( $i = v, s$ , and so), and the Coulomb potential  $V_{\text{Coul}}[r, R_c(\theta', \varphi')]$  as well as the parameters therein have been described in detail in a previous paper [11]. For the sake of clarity and completeness, we give a brief description below.

The employed HF potential,  $V_{\text{HF}}(E)$ , is due to the replacement of a microscopic nonlocal HF potential by a local equivalent. For a Gaussian nonlocality,  $V_{\text{HF}}(E)$  is a linear function of  $E$  for large negative  $E$  and is an exponential for large positive  $E$ . Following Mahaux and Sartor [31], the energy dependence of the Hartree-Fock part of the nuclear mean field is taken as that found by Lipperheide [32]:

$$V_{\text{HF}}(E) = A_{\text{HF}} \exp[-\lambda_{\text{HF}}(E - E_F)], \quad (3)$$

where the parameters  $A_{\text{HF}}$  and  $\lambda_{\text{HF}}$  are undetermined constants and  $E_F$  is the Fermi energy.

The energy dependencies for the imaginary volume term  $W_v(E)$  and the imaginary surface term  $W_s(E)$  are taken as the ones suggested by Brown and Rho [33] and

Delaroche *et al.* [34], respectively, as follows:

$$\begin{aligned}
 W_v(E) &= A_v \frac{(E - E_F)^2}{(E - E_F)^2 + (B_v)^2}, \\
 W_s(E) &= A_s \frac{(E - E_F)^2}{(E - E_F)^2 + (B_s)^2} \exp(-C_s |E - E_F|), \quad (4)
 \end{aligned}$$

where  $A_v$ ,  $B_v$ ,  $A_s$ ,  $B_s$ , and  $C_s$  are undetermined constants.

The isospin dependence of the potential (the Lane term [15,16]) was considered in real  $V_{\text{HF}}(E)$  and imaginary surface  $W_s(E)$  potentials as follows:

$$A_{\text{HF}} = V_0 \left[ 1 + (-1)^{Z+1} \frac{C_{\text{viso}}}{V_0} \frac{N - Z}{A} \right], \quad (5)$$

$$A_s = W_0 \left[ 1 + (-1)^{Z+1} \frac{C_{\text{wiso}}}{W_0} \frac{N - Z}{A} \right], \quad (6)$$

where  $V_0$ ,  $C_{\text{viso}}$ ,  $W_0$ , and  $C_{\text{wiso}}$  are undetermined constants, and  $N$  and  $Z$  are the neutron and atomic numbers of the target nucleus.

The spin-orbit potential is taken in the same functional form used by Koning and Delaroche [2], but contains a dispersive contribution,  $\Delta V_{\text{so}}(E)$  [10,35]:

$$V_{\text{so}}(E) = V_{\text{so}} \exp[-\lambda_{\text{so}}(E - E_F)] + \Delta V_{\text{so}}(E), \quad (7)$$

$$W_{\text{so}}(E) = W_{\text{so}} \frac{(E - E_F)^2}{(E - E_F)^2 + (B_{\text{so}})^2}. \quad (8)$$

The calculations for all dispersive contributions are performed using a dispersion relation as follows:

$$\Delta V(r, E) = \frac{\mathcal{P}}{\pi} \int_{-\infty}^{+\infty} \frac{W(r, E')}{E' - E} dE', \quad (9)$$

where symbol  $\mathcal{P}$  denotes that the principal value of the integral should be taken. Analytical dispersive integrals are calculated following Ref. [36].

In Eq. (4), the imaginary volume potential is assumed to be symmetric about  $E = E_F$ . Such a symmetry assumption holds for small values of  $|E - E_F| \leq E_a$ , but it is no longer valid for large values of  $|E - E_F| > E_a$  [31]. Here  $E_a$  is a constant energy suggested by Mahaux and Sartor to be approximately equal to the depth of the nuclear potential [31]. In that energy region, we adopted a modified (asymmetric) imaginary volume potential as given in Ref. [11] that leads to an additional dispersive volume contribution.  $E_a$  is used as an additional fitting parameter in this work. The derived value of  $E_a = 52$  MeV is close to Mahaux and Sartor’s suggestion of 60 MeV [31].

The Coulomb potential  $V_{\text{Coul}}[r, R_c(\theta', \varphi')]$  is calculated using a multipole expansion of a charged ellipsoid with uniform charge density with the Coulomb radius  $R_c$  and zero outside as suggested by Satchler *et al.* [37]. The spherical term of the Coulomb potential was calculated by taking into account the diffuseness of the charge density distribution of the form  $f_c = [1 + \exp(r - R_c/a_c)]^{-1}$ .

A similar form of the potential as Eq. (1) was used by Capote *et al.* [14]. However, an “effective” proton energy  $E^* = E_p -$

TABLE VII. Dispersive coupled-channels OMP parameters for  $^{54,56,58}\text{Fe}$ , with the SRM Hamiltonian parameters given in Table II and the deformation parameters given in Table V.

	Volume	Surface
Real depth (MeV)	$V_0 = 52.2848 + 0.0292A$ $\lambda_{\text{HF}} = 0.008$ $C_{\text{viso}} = 20.00$ + dispersive	Dispersive
Imaginary (MeV)	$A_v = 12.36$ $B_v = 77.4$ $E_a = 52$	$W_0 = 12.03$ $B_s = 12.64$ $C_s = 0.01355$ $C_{\text{viso}} = 14.00$
Geometry (fm)	$r_{\text{HF}} = 1.2873 - 0.0016A$ $a_{\text{HF}} = 0.504 + 0.00225A$ $r_v = 1.0551$ $a_v = 0.92676 - 0.00021A$	$r_s = 1.0277 + 0.0039A$ $a_s = 0.503$
	Spin-orbit	Coulomb
Real depth (MeV)	$V_{\text{so}} = 6.98$ $\lambda_{\text{so}} = 0.005$ + dispersive	$C_{\text{Coul}} = 1.0$
Imaginary (MeV)	$A_{\text{so}} = -3.1$ $B_{\text{so}} = 160.00$	
Geometry (fm)	$r_{\text{so}} = 1.0388$ $a_{\text{so}} = 0.59$	$r_c = 1.188$ $a_c = 0.32$

$C_{\text{Coul}} \frac{Z}{A^{1/3}}$  is used here for the real potentials. The constant  $C_{\text{Coul}}$  is an adjustable parameter accounting for the effective radius of proton interaction in the nucleus. Note that the constant  $e^2$  in our definition is included in the constant  $C_{\text{Coul}}$ . At this effective energy  $E^*$ , the optical potential can be expanded in a Taylor series as

$$\begin{aligned}
 V(E^*) &= V\left(E - C_{\text{Coul}} \frac{Z}{A^{1/3}}\right) \\
 &= V(E) - C_{\text{Coul}} \frac{Z}{A^{1/3}} \frac{d}{dE}[V(E)] + \dots \quad (10)
 \end{aligned}$$

Equation (10) holds for  $V_{\text{HF}}(E^*)$ ,  $\Delta V_v(E^*)$ , and  $\Delta V_s(E^*)$ . One can see that the first derivative term  $-C_{\text{Coul}} \frac{Z}{A^{1/3}} \frac{d}{dE}[V(E)]$  is just the Coulomb correction term used in previous works [11,14,38]. In fact, Eq. (10) is a generalization of previously used Coulomb correction with the consideration of the full Coulomb correction in all orders. This energy shift has been applied to the real potential only (denoted by  $E^*$ ); therefore the potential is not fully charge independent. We can speak of the approximate Lane consistency as previously discussed for actinides in Ref. [17].

For the sake of simplicity, the energy-independent potential geometry is used, but small  $A$  dependence of the geometry parameters was introduced to derive a regional potential.

The DCCOM potential parameters were searched to fit the experimental proton and neutron scattering data by minimizing the quantity  $\chi^2$  in a usual way [19]. All experimental data used in the fitting process are taken from the EXFOR database [39]. In total we adjusted 15 parameters from the real volume potential, the surface and volume absorptive potential, the spin-orbit potential, and the Coulomb interaction, namely,  $V_0$ ,

$\lambda_{\text{HF}}$ ,  $C_{\text{viso}}$ ,  $A_v$ ,  $B_v$ ,  $E_a$ ,  $W_0$ ,  $B_s$ ,  $C_s$ ,  $C_{\text{viso}}$ ,  $V_{\text{so}}$ ,  $\lambda_{\text{so}}$ ,  $A_{\text{so}}$ ,  $B_{\text{so}}$ , and  $C_{\text{Coul}}$ , and 10 energy-independent geometric parameters, namely,  $r_{\text{HF}}$ ,  $a_{\text{HF}}$ ,  $r_v$ ,  $a_v$ ,  $r_s$ ,  $a_s$ ,  $r_{\text{so}}$ ,  $a_{\text{so}}$ ,  $r_c$ , and  $a_c$ . They allow the best fit to the experimental data and are summarized in Table VII.

We assumed that parameters  $V_0$ ,  $r_{\text{HF}}$ ,  $a_{\text{HF}}$ ,  $a_v$ , and  $r_s$  are linearly dependent on mass number  $A$ . However this dependence is found to be quite weak, which implies that the derived regional potential for Fe isotopes can be extended to neighboring nuclei. The energy and mass number dependen-

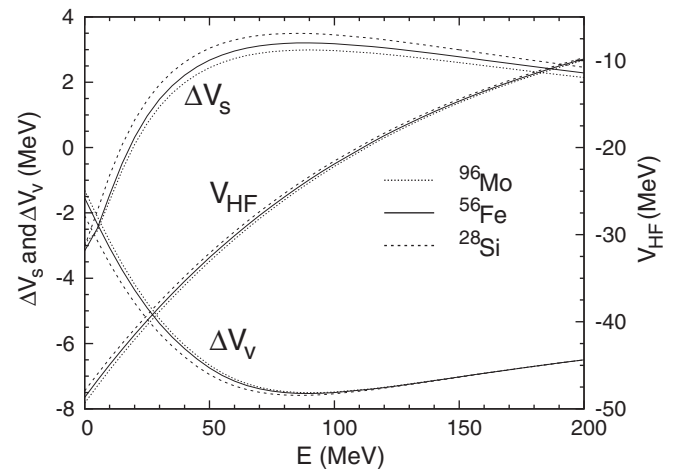


FIG. 3. Dependencies on energy and mass number for the real volume  $V_{\text{HF}}(E)$ , the real dispersive-volume contribution  $\Delta V_v$ , and the real dispersive-surface potential  $\Delta V_s$  for  $^{28}\text{Si}$ ,  $^{56}\text{Fe}$ , and  $^{96}\text{Mo}$  nuclei.  $V_{\text{HF}}(E)$  is scaled on the right, while  $\Delta V_s$  and  $\Delta V_v$  are scaled on the left.

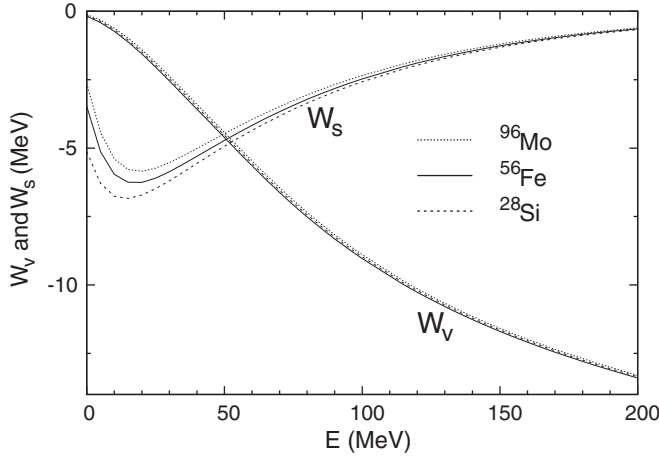


FIG. 4. Volume and surface imaginary potential depths for  $^{28}\text{Si}$ ,  $^{56}\text{Fe}$ , and  $^{96}\text{Mo}$ .

cies of the real volume potential  $V_{\text{HF}}(E)$  and the corresponding dispersive contribution  $\Delta V_v(E)$ , as well as the surface dispersive contribution  $\Delta V_s$ , are shown in Fig. 3 for the cases of  $^{28}\text{Si}$ ,  $^{56}\text{Fe}$ , and  $^{96}\text{Mo}$  to study the mass dependence of derived OMPs. A similar comparison is given in Fig. 4 for imaginary potentials.

It can be seen from Figs. 3 and 4 that the dependencies of  $V_{\text{HF}}$ ,  $W_v$ , and  $\Delta V_v$  on mass number are weak within a wide mass range. However, for the imaginary surface potential  $W_s$  and the corresponding real dispersive-surface contribution  $\Delta V_s$ , the dependencies are stronger, deviating from  $^{56}\text{Fe}$  by less than 10%. Calculated DCCOM results for the iron group nuclei are presented under Results and Discussion.

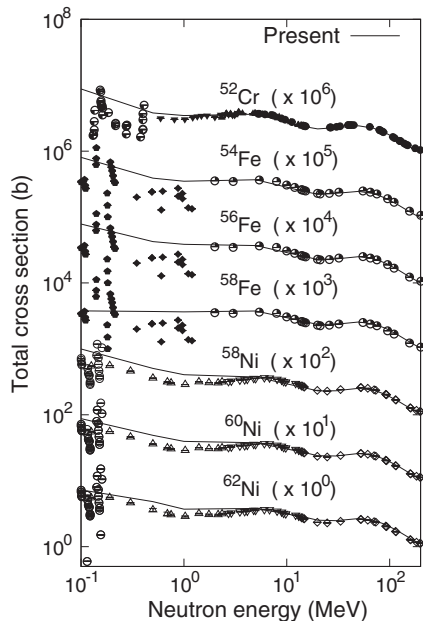


FIG. 5. Comparison of neutron total cross sections with measurements.

#### IV. A COMPUTATIONAL METHOD FOR ANALYZING POWER

In this work a computational method to derive the analyzing power in the actual coupled-channels calculations has been given following the formalism for a polarization vector developed by Tamura in his canonical work [18].

It is assumed that initially both the projectile and the target are in some polarized states described by amplitudes  $a_{m_s}^{(i)}$  and  $b_{M_1}^{(i')}$ , respectively. Here the superscripts  $i$  and  $i'$  specify different spin ensembles. Then, the polarization vector  $P_n(\theta, \phi)$ , parallel to a given unit vector  $\vec{n}$  (the normal to the scattering plane) of the particle scattered in the direction specified by the polar angles  $(\theta, \phi)$ , is given in Eq. (50) in Ref. [18] as

$$\begin{aligned} \sigma_n^{(s)}(\theta, \phi) \vec{P}_n(\theta, \phi) &= \sum_{ii'} \sum_{(m)} X_{m_s M_1; m'_s M_n}^*(\theta, \phi) X_{\bar{m}_s \bar{M}_1; \bar{m}'_s \bar{M}_n}(\theta, \phi) \\ &\times \langle m'_s | (\vec{\sigma} \cdot \vec{n}) | \bar{m}'_s \rangle a_{m_s}^{(i)*} b_{M_1}^{(i')} a_{\bar{m}_s}^{(i)} b_{\bar{M}_1}^{(i')}, \end{aligned} \quad (11)$$

where the summation  $\sum_{(m)}$  is over all projections (magnetic quantum numbers). Note that the subsequent explanations follow the same symbol definitions used by Tamura, except for new quantities.  $\sigma_n^{(s)}(\theta, \phi)$  is the shape differential cross section with the target in its  $n$ th state, and  $\vec{\sigma}$  is the Pauli spin matrix. The amplitude  $X_{m_s M_1; m'_s M_n}(\theta, \phi)$  given by Eq. (48) in Ref. [18] describes the scattering probability from the initial state with  $m_s$  and  $M_1$  to the final state with  $m'_s$  and  $M_n$  quantum numbers. For the case of unpolarized projectile and unpolarized target, the amplitudes  $a_{m_s}^{(i)}$  and  $b_{M_1}^{(i')}$  can be simplified as  $a_{\frac{1}{2}}^{(1)} = a_{-\frac{1}{2}}^{(2)} = (\frac{1}{2})^{\frac{1}{2}}$ ,  $a_{-\frac{1}{2}}^{(1)} = a_{\frac{1}{2}}^{(2)} = 0$ , and  $b_{M_1}^{(N_1)} = (\frac{1}{I_1}) \delta_{M_1, N_1}$ ,  $M_1, N_1 = -I_1, \dots, I_1$ . Correspondingly, Eq. (11) is considerably simplified, but it is still hard to use such an equation in actual coupled-channels calculations.

We restrict our discussion to the calculation of the  $y$  component  $P_n^y(\theta, \phi)$  of the polarization vector  $\vec{P}_n(\theta, \phi)$ , because the  $y$  component  $A_y(\theta)$  of the analyzing power vector  $\vec{A}$  is usually measured. Here, the  $y$  axis is chosen as the normal to the scattering plane. Correspondingly, the matrix elements  $\langle m'_s | (\vec{\sigma} \cdot \vec{n}) | \bar{m}'_s \rangle$  can be simplified as  $\langle m'_s | \sigma_y | \bar{m}'_s \rangle$ , where  $\sigma_y$  is the  $y$  component of the Pauli matrix. These  $y$ -component matrix elements can be evaluated by  $2 \times 2$  combinations of two spin functions:  $|m_s\rangle$  and  $|\bar{m}_s\rangle$ . With such a treatment and the consideration of symmetry in the azimuthal angle  $\phi$ , Eq. (11) leads to

$$\begin{aligned} \sigma_n^{(s)}(\theta) P_n^y(\theta) &= \frac{1}{2\hat{I}_1^2} \sum_{m_s M_1 M_n} 2\text{Im}[X_{m_s M_1; \frac{1}{2} M_n}^*(\theta) X_{m_s M_1; -\frac{1}{2} M_n}(\theta)], \end{aligned} \quad (12)$$

where the differential cross sections  $\sigma_n^{(s)}(\theta)$  are reduced from Eq. (49) in Ref. [18] to

$$\sigma_n^{(s)}(\theta) = \frac{1}{2\hat{I}_1^2} \sum_{m_s M_1 m'_s M_n} |X_{m_s M_1; m'_s M_n}(\theta)|^2. \quad (13)$$

In our coupled-channels calculations, the Coulomb amplitude  $f_c(\theta)$  and  $C$ -matrix elements included in the expression of the amplitude  $X_{m_s M_1; m'_s M'_1}(\theta)$  are evaluated by OPTMAN [25] code. Meanwhile,  $\sigma_n^{(s)}(\theta)$  are just the elastic and inelastic angular distributions.

Equation (12) can be used to calculate both elastic and inelastic  $y$ -component polarizations. For the case of elastic scattering, it is well known that the asymmetry (analyzing power) of the reaction induced by the completely polarized particle is equal to the polarization produced in the (time-)reversed reaction initiated by unpolarized particles [40]. Therefore,  $P_n^y(\theta)$  ( $n = 1$ ) is equivalent to the analyzing power  $A_y(\theta)$ . For the inelastic case both formulations are not equal in the general case [41]. However, it has been shown [41,42] that the polarization and the asymmetry (analyzing power) are equal in distorted-wave Born approximation (DWBA) calculations within an adiabatic approximation (i.e., when the projectile energy is much higher than the level energy, leading to a weak coupling limit). We found a similar behavior for the strong coupling case in coupled-channels calculations. Numerical values calculated with the ECIS code [43] using both formulations display very good agreement, with only minor differences observed at backward angles. Therefore, it is reasonable to assume that  $P_n^y(\theta)$  can be used for comparison with experimental  $A_y(\theta)$  data. Further investigations of the inelastic analyzing power are warranted.

## V. RESULTS AND DISCUSSION

This section shows the results of total cross sections, proton reaction cross sections, nucleon elastic/inelastic angular distributions,  $(p, n)$  data, and analyzing powers, mainly for

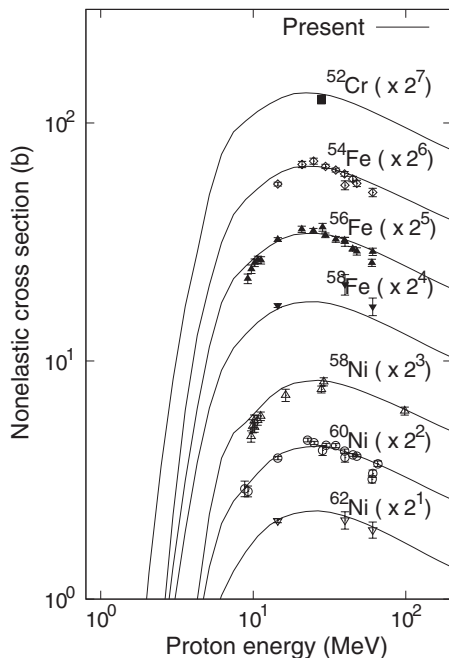


FIG. 6. Comparison of proton nonelastic cross sections with measurements.

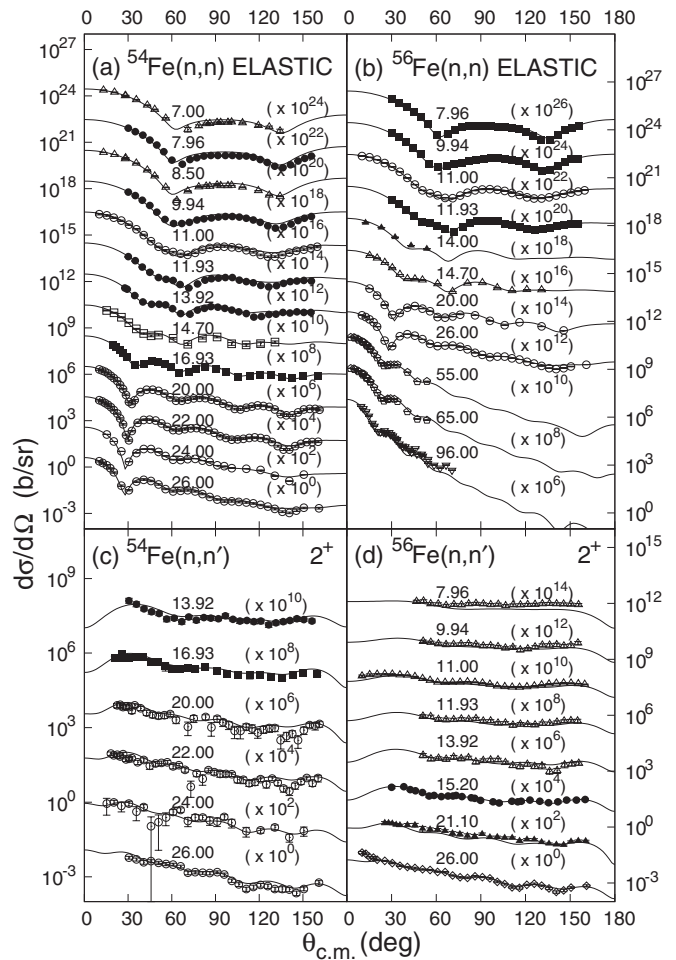


FIG. 7. Comparison of neutron elastic and inelastic scattering angular distributions with measurements for Fe isotopes at different incident energies.

Fe isotopes. Selected results for Ni isotopes and  $^{52}\text{Cr}$  are also presented showing the predictive power of the derived regional DCCOM potential.

Figures 5 and 6 present predictions of neutron total cross sections and proton nonelastic cross sections for Fe-group nuclei up to 200 MeV, respectively. It is seen that the neutron total cross sections are in good agreement with experimental data from 1 to 200 MeV. The deviation of our predictions from the experiments is on average within 5% above 1 MeV. Only at energies below 1 MeV does the prediction clearly deviate from the experimental data. However, it is not expected that the present potential will reproduce the total cross sections at low energies very precisely, because resonance structures often appear in the low-energy ranges, which are beyond the average description assumed by the optical model. Similarly, good agreement with measurement is seen for proton nonelastic cross sections. On average, the difference between the calculation and the measurement is within 5%.

The nucleon elastic and inelastic scattering angular distributions for Fe isotopes are shown in Figs. 7 and 8, respectively.

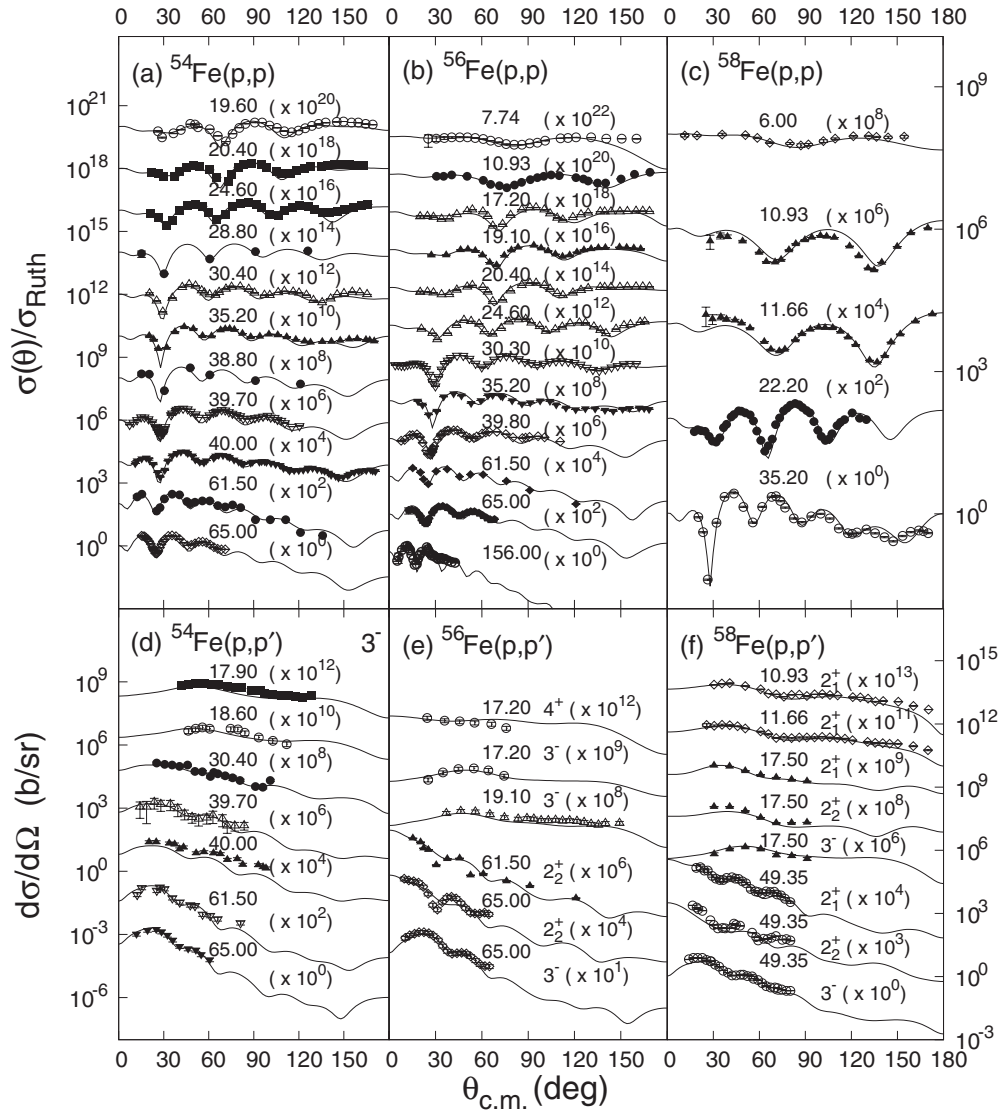


FIG. 8. Same as Fig. 7, but for protons.

Obviously, the predictions for both neutron and proton elastic scattering describe the experimental data rather well over the entire energy and angular range. The same is generally true for neutron and proton inelastic scattering on  $3^-$ ,  $4^+$ , and  $2^+$  excited levels. The exception is an observed slight underestimation for the  $2^+$  level of the  $^{56}\text{Fe}(n, n')$  reaction at 7.96 MeV in Fig. 7, perhaps due to the missing compound-inelastic contribution. A slight underestimation for the  $3^-$  level of the  $^{54}\text{Fe}(p, p')$  reaction at 40 MeV is also seen in Fig. 8. The reason might be due to some problems with experimental data (for instance, the subtraction of contributions from other levels, because the  $3^-$  level contribution is relatively smaller than the others and such subtraction may give large errors). Our calculations show good agreement for scattering data on the  $3^-$  level at all other energies.

The results of the  $(p, n)$  transition exciting the ground state IAS and  $2^+$  EAS are shown in Fig. 9 for Fe isotopes,  $^{52}\text{Cr}$ , and  $^{58,62}\text{Ni}$ . An overall agreement with measurements is seen for

all energies and the whole angular region, with the exceptions of forward angles for the  $2^+$  state of the  $^{58}\text{Fe}(p, n)$  reaction at 120 MeV. Note that experimental  $(p, n)$  data were not used in the fitting of our optical potential parameters. Even so, it is very satisfactory that the DCCOM potential can describe these data rather well to such an extent. This demonstrates the approximate Lane consistency of the derived potential.

Figure 10 shows the neutron and proton elastic analyzing powers  $A_y$  calculated for Fe isotopes, along with the experimental data and those corresponding to the spherical optical model calculated by TALYS code [44] with the Koning-Delaroché potential [2]. Our calculations for neutrons are in excellent agreement with data, while the results for proton elastic  $A_y$  are also satisfactory, except for a slightly poor description at backward angles for  $^{54}\text{Fe}$  at 10 MeV. It is observed that our calculations are, in general, consistent with TALYS spherical optical-model calculations. However, a slight shift between both calculations can be seen at some energies.

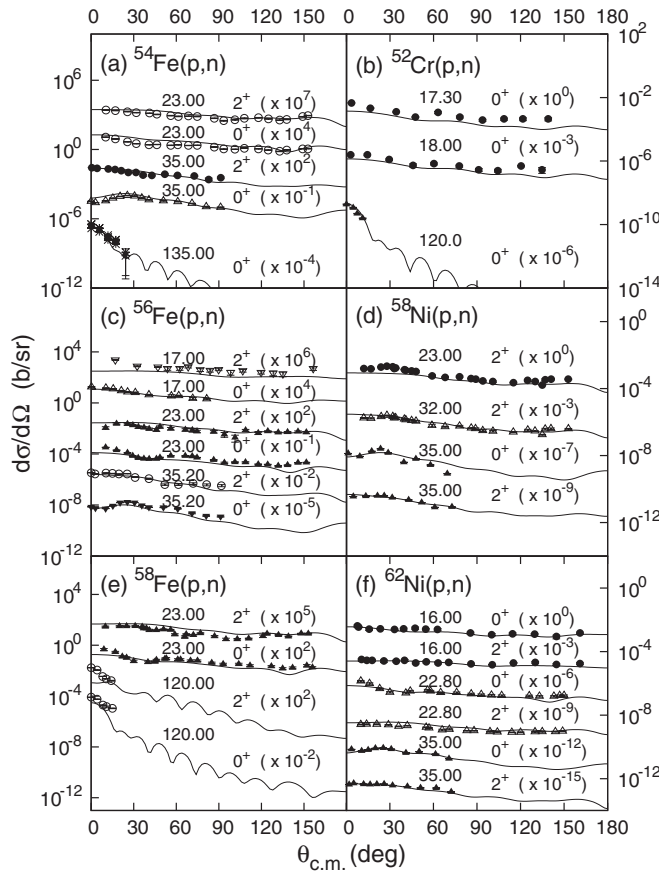


FIG. 9. Predictions for  $(p, n)$  transition exciting IAS and EAS states for Fe isotopes (left) and three other nuclei (right) at different incident energies and levels.

TALYS calculations show an irregular smooth pattern  $65^\circ$  at 65 MeV, contrary to our oscillation pattern.

The predictions for neutron and proton inelastic  $A_y$  for Fe isotopes are presented in Fig. 11, compared with DWBA results. TALYS drives the ECIS code [43] to perform such DWBA calculations. The results for neutrons are rather good, while the results for protons are also good including the inelastic polarization for  $3^-$  and  $2_1^+$  states. However, they are of somewhat lower quality than those for neutrons, with slight underestimation seen near extrema for the cases of the  $2_1^+$  state of  $^{54}\text{Fe}(p, p')$  at 18.6 MeV, as well as for the  $2_1^+$  state of  $^{56}\text{Fe}(p, p')$  at 65 MeV.

It is expected that the DCCOM is a better approximation (due to the strong coupling of collective levels) than DWBA (weak coupling) at lower excitation energies. Indeed, DCCOM results are slightly better than DWBA ones, although both results describe relatively well the experimental data. A similar situation is seen as shown in Fig. 10; that is, a shift between both results at some energies is observed, and the DWBA results display an irregular smooth pattern above  $65^\circ$  at 65 MeV.

The new option implemented in the OPTMAN code [25] allows calculating elastic and inelastic  $A_y$  for both even-even and odd nuclei. We also used our derived DCCOM potential

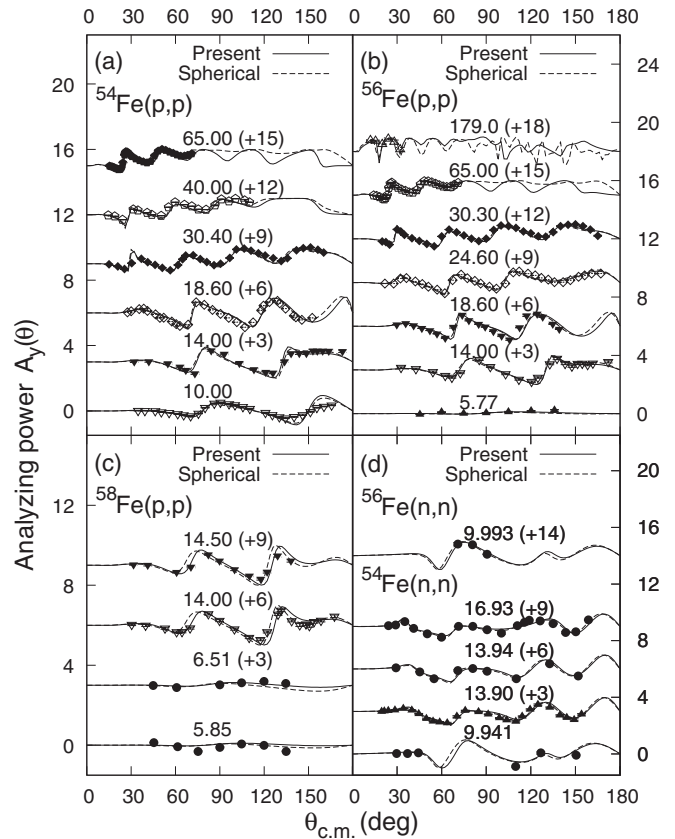


FIG. 10. Neutron and proton elastic analyzing powers for Fe isotopes, compared with the experimental data and TALYS calculations using a Koning-Delaroche potential.

to predict the measured proton elastic  $A_y$  data, as shown in Fig. 12, for the odd nucleus  $^{57}\text{Fe}$ . Note that, for the case of the odd- $A$  nucleus  $^{57}\text{Fe}$ , the coupled-channels calculation is based on the rigid-rotor model with the deformation parameter  $\beta_2$  being 0.2017,  $\beta_4$  being 0.0158, and  $\beta_6$  being  $-0.0071$ . The agreement of our calculations with the measurements is satisfactory. This OMP extension to odd nuclei is important for applications, because the same OMP can be used for all iron isotopes, eliminating inconsistencies in calculated reaction cross sections between odd and even isotopes. Unfortunately, few experimental inelastic data for odd- $A$  nuclei are available, so it is hard to make a further test of the applicability of this approach.

Finally, we present some additional results of the elastic and inelastic analyzing powers for  $^{58}\text{Ni}$  in Fig. 13 to show the predictive power of our potential. As before, one can see that calculated results for elastic  $A_y$  reproduce well the experimental data at all energies. The description for inelastic  $A_y$  is also good and reproduces the experimental data for all states, except the poor agreement with data measured at 178 MeV. Our description reproduces well the main tendencies of experimental data, but predicts narrow oscillations and deeper minima at higher energies. Those predicted minima are not observed in the experiments, but such narrow oscillations might be difficult to measure due to degraded experimental

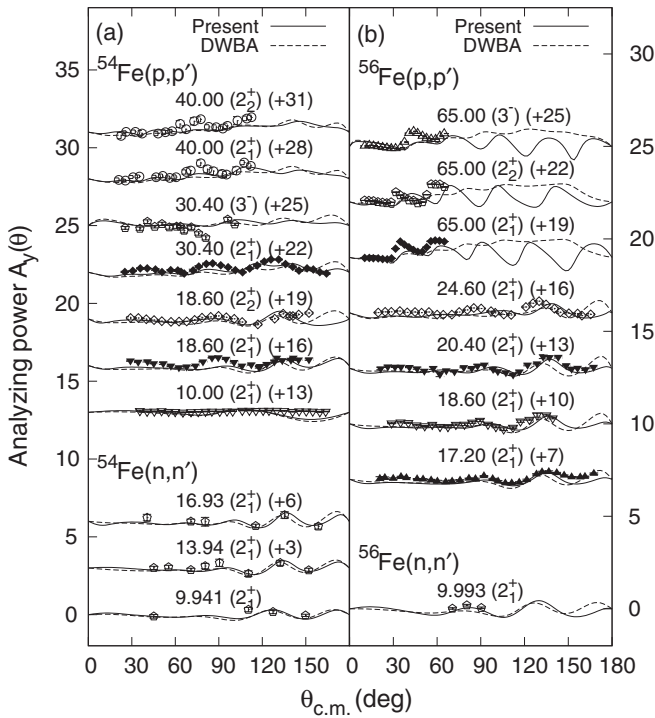


FIG. 11. Same as Fig. 10, but for inelastic analyzing powers. DWBA results calculated with TALYS are also shown for comparison.

resolution at higher energies. New experimental data at higher energies are welcome for further investigations.

It should be mentioned that the inclusion of the dispersive negative contribution  $\Delta V_{so}(E)$  to the real spin-orbit potential is compensated by the observed increase in the real potential term compared to the original Koning-Delaroche spin-orbit parametrizations [2].  $A_y(\theta)$  calculations for studied isotopes are weakly dependent on the employed spin-orbit model, making it difficult to choose between different spin-orbit models. However, a dispersive spin-orbit potential is a nat-

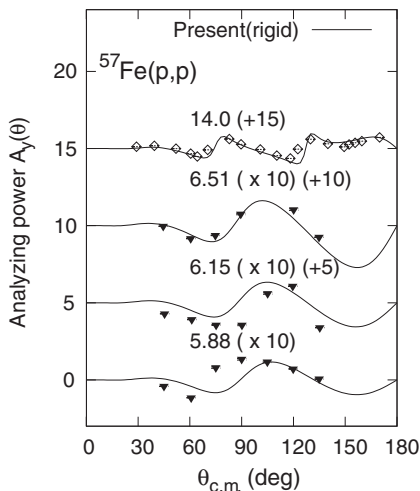


FIG. 12. Comparison of proton elastic analyzing powers with measurements for  $^{57}\text{Fe}$ .

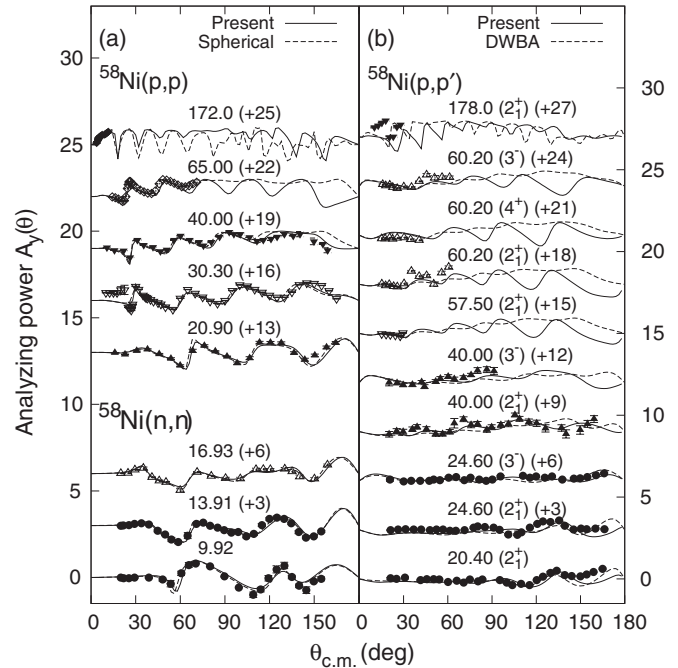


FIG. 13. Comparison of nucleon elastic and inelastic scattering analyzing powers for  $^{58}\text{Ni}$  with the experimental data, along with TALYS calculations including DWBA results.

ural consequence of a consistent consideration of dispersive relations in our approach.

## VI. SUMMARY AND CONCLUSIONS

An approximate Lane-consistent dispersive coupled-channels OMP is obtained for iron-group nuclei. This potential shows a very good description of available nucleon-nucleus scattering data up to 200 MeV, including neutron total cross sections, proton nonelastic cross sections, and nucleon elastic and inelastic scattering angular distributions. Additionally, a very good prediction of quasielastic scattering ( $p, n$ ) data and elastic and inelastic analyzing powers was achieved. In conclusion, this potential works well for almost all the nucleon interaction data for Fe isotopes. Particularly the level of agreement with ( $p, n$ ) data validates the OMP isovector component and shows the approximate Lane consistency of the derived OMP. Meanwhile the agreement with analyzing power data shows the reliability of the employed dispersive spin-orbit potential.

## ACKNOWLEDGMENTS

R.L. and W.S. wish to thank professors Q. B. Shen and B. A. Zhang for valuable discussions. This work is partially supported by the National Natural Science Foundation of China (Grant No. 91226104) and ISTC Project B-1804. The work of one of the authors (J.M.Q.) was supported by the Spanish Plan Nacional de I+D+i under Contracts No. FPA2011-28770-C03-02 and No. FIS2011-28738-C02-01.

- [1] R. Capote *et al.*, *Nucl. Data Sheets* **110**, 3107 (2009) (see also [www-nds.iaea.org/RIPL-3/](http://www-nds.iaea.org/RIPL-3/)).
- [2] A. J. Koning and J. P. Delaroche, *Nucl. Phys. A* **713**, 231 (2003).
- [3] C. Mahaux and H. Ngo, *Nucl. Phys. A* **431**, 486 (1984).
- [4] C. Mahaux and R. Sartor, *Phys. Rev. Lett.* **57**, 3015 (1986).
- [5] C. Mahaux and R. Sartor, *Adv. Nucl. Phys.* **20**, 1 (1991).
- [6] B. Morillon and P. Romain, *Phys. Rev. C* **74**, 014601 (2006).
- [7] O. V. Bespalova *et al.*, *Bull. Russ. Acad. Sci.: Phys.* **71**, 428 (2007).
- [8] O. V. Bespalova, T. A. Ermakova, E. A. Romanovskii, T. I. Spasskaya, and A. A. Klimochkina, *Bull. Russ. Acad. Sci.: Phys.* **73**, 816 (2009).
- [9] W. H. Dickhoff, D. Van Neck, S. J. Waldecker, R. J. Charity, and L. G. Sobotka, *Phys. Rev. C* **82**, 054306 (2010).
- [10] B. Morillon and P. Romain, *Phys. Rev. C* **70**, 014601 (2004).
- [11] E. Sh. Soukhovitskiĭ, R. Capote, J. M. Quesada, and S. Chiba, *Phys. Rev. C* **72**, 024604 (2005).
- [12] R. Capote, E. Sh. Soukhovitskiĭ, J. M. Quesada, and S. Chiba, *Phys. Rev. C* **72**, 064610 (2005).
- [13] S. Kunieda, S. Chiba, K. Shibata, A. Ichihara, and E. Sh. Sukhovitskiĭ, *J. Nucl. Sci. Technol.* **44**, 838 (2007).
- [14] R. Capote, S. Chiba, E. Sh. Soukhovitskiĭ, J. M. Quesada, and E. Bauge, *J. Nucl. Sci. Technol.* **45**, 333 (2008).
- [15] A. M. Lane, *Phys. Rev. Lett.* **8**, 171 (1962).
- [16] A. M. Lane, *Nucl. Phys.* **35**, 676 (1962).
- [17] J. M. Quesada, R. Capote, E. Sh. Soukhovitskiĭ, and S. Chiba, *Phys. Rev. C* **76**, 057602 (2007).
- [18] T. Tamura, *Rev. Mod. Phys.* **37**, 679 (1965).
- [19] E. Sh. Sukhovitskiĭ, Y.-O. Lee, J. Chang, S. Chiba, and O. Iwamoto, *Phys. Rev. C* **62**, 044605 (2000).
- [20] J.-Y. Lee, E. Sh. Sukhovitskiĭ, Y.-O. Lee, J. Chang, S. Chiba, and O. Iwamoto, *J. Korean Phys. Soc.* **38**, 88 (2001).
- [21] E. Sh. Soukhovitskiĭ, S. Chiba, J.-Y. Lee, Y.-O. Lee, J. Chang, T. Maruyama, and O. Iwamoto, *J. Nucl. Sci. Technol.* **39**, 816 (2002).
- [22] E. Sh. Soukhovitskiĭ, S. Chiba, J.-Y. Lee, B. T. Kim, and S. W. Hong, *J. Nucl. Sci. Technol.* **40**, 69 (2003).
- [23] S. Chiba, O. Iwamoto, Y. Yamanouti, M. Sugimoto, M. Mizumoto, K. Hasegawa, E. Sh. Soukhovitskiĭ, Y. V. Porodzinskiĭ, and Y. Watanabe, *Nucl. Phys. A* **624**, 305 (1997).
- [24] W. Greiner and J. A. Maruhn, *Nuclear Models* (Springer-Verlag, Berlin, Heidelberg, 1996).
- [25] E. Sh. Soukhovitskiĭ, S. Chiba, O. Iwamoto, K. Shibata, T. Fukahori, and G. B. Morogovskii, Programmes OPTMAN and SHEMMAN, Version 8, Technical Report JEARI-Data/Code 2005-002, Japan Atomic Energy Research Institute, Ibaraki, Japan, 2005, Supplement to OPTMAN code manual, Version 10 (2008).
- [26] S. Raman, C. H. Malarkey, W. T. Milner, C. W. Nestor, P. H. Stelson, *At. Data Nucl. Data Tables* **36**, 1 (1987).
- [27] R. H. Spear, *At. Data Nucl. Data Tables* **42**, 55 (1989).
- [28] W. Sun, Y. Watanabe, E. Sh. Soukhovitskiĭ, O. Iwamoto, and S. Chiba, *J. Nucl. Sci. Technol.* **40**, 635 (2003).
- [29] A. D. Anderson, C. Wong, and J. W. McClure, *Phys. Rev.* **138**, B615 (1965).
- [30] G. C. Jon, H. Orihara, C. C. Yun, A. Terakawa, K. Itoh, A. Yamamoto, H. Suzuki, H. Mizuno, G. Kamurai, K. Ishii, and H. Ohnuma, *Phys. Rev. C* **62**, 044609 (2000).
- [31] C. Mahaux and R. Sartor, *Nucl. Phys. A* **528**, 253 (1991).
- [32] R. Lipperheide, *Z. Phys.* **202**, 58 (1967).
- [33] G. E. Brown and M. Rho, *Nucl. Phys. A* **372**, 397 (1981).
- [34] J. P. Delaroche, Y. Wang, and J. Rapaport, *Phys. Rev. C* **39**, 391 (1989).
- [35] R. L. Walter, in *Proceedings of the Specialists Meeting on Nucleon-Nucleus Optical Model up to 200 MeV, Bruyères-le-Châtel, France, 1997* p. 199. Available online at [www.nea.fr/html/science/om200/](http://www.nea.fr/html/science/om200/).
- [36] J. M. Quesada, R. Capote, A. Molina, M. Lozano, and J. Raynal, *Phys. Rev. C* **67**, 067601 (2003).
- [37] R. H. Bassel, R. M. Drisko, and G. R. Satchler, Technical Report ORNL-3240, Oak Ridge National Laboratory, 1962.
- [38] L. Hao, W. Sun, and E. Sh. Soukhovitskiĭ, *J. Phys. G: Nucl. Part. Phys.* **35**, 095103 (2008).
- [39] EXchange FORmat database (EXFOR) is maintained by the Network of Nuclear Reaction Data Centers (see [www-nds.iaea.org/nrdc/](http://www-nds.iaea.org/nrdc/)). Data available online (e.g., at [www-nds.iaea.org/exfor/](http://www-nds.iaea.org/exfor/)).
- [40] T. Y. Wu and T. Ohmura, *Quantum Theory of Scattering* (Prentice Hall, New York, 1962).
- [41] G. R. Satchler, *Phys. Lett.* **19**, 4 (1965).
- [42] H. Sherif, *Can. J. Phys.* **49**, 983 (1971).
- [43] J. Raynal, in *Computing As a Language of Physics, ICTP International Seminar Course, Trieste, Italy*, International Atomic Energy Agency, Vienna, Austria, 1971, p. 281; in *Proceeding of Specialists Meeting on Nucleon-Nucleus Optical Model to 200 MeV, Bruyères-le-Châtel, France, 1997*, p. 159 (see also [www.nea.fr/html/science/om200/](http://www.nea.fr/html/science/om200/)). ECIS code is distributed by the NEA Data Bank.
- [44] A. J. Koning, S. Hilaire, and M. C. Duijvestijn, available online at [www.talys.eu](http://www.talys.eu).